A novel laser powder bed fusion Al-Fe-Zr alloy for superior strength-conductivity trade-off

Camille Pauzon[a,*], Maxence Buttard[a], Arthur Després[a], Béchir Chehab[b], Jean-Jacques Blandin[a], Guilhem Martin[a]

[a]Université Grenoble Alpes, CNRS, Grenoble INP, SIMaP, 38000, Grenoble, France
[b]Constellium Technology Center, Parc économique Centr'Alp, 38341, Voreppe, France

*Corresponding author : camille.pauzon@simap.grenoble-inp.fr

ABSTRACT

New aluminium alloy design strategies for laser powder bed fusion (LPBF) are needed to target high strength and conductivity applications and substitute the traditional 6xxx series which suffers from hot cracking during LPBF processing. This study presents the route followed to design a novel Al-Fe-Zr alloy offering good processability, superior yield strength (310 MPa) and thermal conductivity (180 W/m·K) after direct ageing (400°C/4h). The multi-scale characterization, combining scanning and transmission electron microscopy with automated crystallographic orientation mapping and energy dispersive spectroscopy, reveals the precipitation of plate-like $Al_{13}Fe_4$ and coherent Al_3Zr-$L1_2$ nanoprecipitates upon ageing, enhancing the material's strength. In turn, the associated solid solution depletion results in a significant conductivity increase. The strategy to select low vapour pressure elements and slow diffusers in Al, as well as the low solubility of Fe in Al demonstrates the ability through alloy design for additive manufacturing to fill gaps in the material property space.

Keywords: Additive manufacturing; Laser powder bed fusion; Alloy design; Aluminium alloys; mechanical performance; electrical conductivity.

Combining low density, high corrosion resistance and desirable physical and mechanical properties, Al-alloys are a workhorse of the transport and energy industries. Laser powder bed fusion (LPBF) offers new perspectives to achieve near-net shape complex components in few manufacturing steps, compared to the traditional routes of cast and wrought products.

The preferred approach to produce Al-based LPBF components has been to use casting alloys [1], for example AlSi7Mg and AlSi10Mg. Unfortunately, these grades do not deliver high mechanical performance when LPBF-processed [2,3]. Al-alloys from the 6xxx series provide both good strength and conductivity after a T6 heat-treatment and would be excellent candidates to manufacture heat exchangers. However, they suffer from hot cracking during autogenous laser welding because of their large freezing range and coefficient of thermal expansion [4], and hot cracking also occurs during LPBF [5–8]. Uddin *et al.*[9] managed to suppress hot cracking using powder bed heating to 500°C. Despite its success, this approach is not compatible with industrial LPBF systems. Besides, adjustments to the alloy composition have been considered, with addition of grain refiners that promote the heterogeneous nucleation of Al grains, making the alloy more resistant to cracking. These refiners can either be inoculating agents admixed to the powder like TiB_2 and TiC [10,11], or primary phases formed in situ such as Al_3X (X=Zr, Sc) [5,6,8,12]. In this case, the benefit is two-fold with the additional potential for precipitation strengthening through post-ageing treatment [13,14]. It has also been suggested to tune the powder composition to favour elements which do not increase the solidification range [15,16]. These approaches have addressed to some extent the cracking issues of the 6xxx series. But other challenges remain, connected to laser-induced solute evaporation and the need for further solutionizing and quenching. Briefly, there is a necessity to develop novel Al-alloys with strength and conductivity comparable or surpassing that of the 6xxx series combined with good LPBF processability.

This work introduces a new Al-alloy designed for LPBF to achieve a superior strength – conductivity trade-off, by leveraging the unique characteristics of the process: the relatively high solid-liquid interface velocities and high thermal gradients resulting in high cooling rates. The multiscale characterization reveals unique microstructural features of the Al-Fe-Zr alloy inherited from LPBF and their evolution upon ageing, further connected to the material tensile response and conductivity.

One criterion for alloying element selection is a low vapour pressure in comparison to common solutes like Zn and Mg, which tend to restrict the processing window to low energy inputs. The loss of such elements can lead to local composition variations and for example reduced precipitation hardening for 6xxx or 7xxx alloys. Their vaporization can affect the melt pool stability, lead to porosity formation, and generated vapours may interact with the laser, resulting in diminished and varying energy input. These challenges will become more predominant as production capacities are boosted with high power, multi-laser systems, and high layer thicknesses [17]. An additional criterion is to favour elements with low diffusivity in Al to limit the extent of in situ precipitation during thermal cycles and retain a supersaturated solution in the as-built state. Finally, toxic elements such as Be are avoided as well as certain Critical Raw Materials (CRMs) like Sc bringing high costs and supply risks.

With these criteria, Zr and Fe were shortlisted as they combine both low vapour pressure and low diffusivity in solid Al. Zr plays a dual role with the formation of primary Al_3Zr resulting in grain refinement, limiting hot cracking, and its contribution to precipitation strengthening through post-ageing treatment [18]. It diffuses in Al more slowly than Sc [19].

Similarly, Fe exhibits a low diffusivity in Al [20]. Fe is of special interest for its very low equilibrium solubility in Al (0.044 wt.% at 654°C, computed with Thermo-Calc, TCAL6). Its minor content in the solid solution is expected to not significantly reduce the matrix conductivity. In addition, from Scheil-Gulliver calculations, Fe is expected to form $Al_{13}Fe_4$ (Fig. S1). Based on this rationale, gas atomised powder with chemical composition given in **Table 1** was produced. This alloy is designed and supplied by Constellium under the trademark Aheadd® CP1. A particle size between 26 µm (D_{10}) and 64 µm (D_{90}) was measured following ISO 13320.

Element	**Wt. %**	**Method**
Al	Balance	N. A.
Fe	1.02	ICP
Zr	1.05	ICP
O	0.098	LECO
N	<0.005	LECO
H	0.0019	LECO

Table 1: Chemical composition of the Al-Fe-Zr alloy gas atomised powder for LPBF, measured by inductively coupled plasma optical emission spectrometry (ICP) and carrier gas hot extraction (LECO).

Samples were produced with an EOS M290 under Argon. The baseplate made of a 5XXX-serie Al-alloy was preheated to 100°C, and the stripe scanning pattern was rotated by 67° between layers. Using a 370 W power, a 1400 mm/s scan speed, 0.13 mm hatch distance and a 60 µm layer thickness, near-fully-dense samples (> 99.7 %) were manufactured. The specimens were heat treated for stress-relief at 300°C for 2 hours before baseplate removal. Such stress-relief post-processing is commonly applied to LPBF Al components to avoid unwanted deformation, see e.g. [21,22]. Samples were then subjected to a post-fabrication ageing treatment at 400°C for 4 hours, identified as the peak ageing with 110 ± 2 HV, vs. 65 ± 2 HV after stress-relief. The low diffusivity of Zr in the matrix explains the high ageing temperature.

Microstructure characterization was performed using a scanning electron microscope (Zeiss Gemini SEM 500 FEG) equipped with an electron backscattered diffraction (EBSD) detector. The samples were polished until a 1µm diamond suspension step, and a final vibratory polishing. EBSD maps were acquired with a 0.3 µm step size at 20 kV. High angle grain boundaries plotted in black on the orientation maps are defined by a misorientation >10°. The MATLAB toolbox MTex was used to compute the grain sphericity defined as the ratio of the grain area to the product of the perimeter and equivalent radius (equal to 0.5 for a perfect circle).

Transmission electron microscopy (TEM) was conducted with a TEM FEG JEOL 2100 and perform energy-dispersive X-ray spectroscopy (EDS) by operating at 200 kV. Thin foils were prepared by electropolishing using a solution of 30% nitric acid and 70% methanol at -35°C and 20V. Phase and orientation information of specific location identified at the melt pool scale were retrieved using ACOM (Automated Crystallographic Orientation Mapping) with the ASTAR™ hardware and software from Nanomegas. This technique presented in [23] and applied to LPBF materials [16,24], consists in scanning the region of interest with a nano-beam and collecting for each point the diffraction pattern acquired by a CCD camera. This diffraction dataset is post-processed, to compare the diffraction pattern in each point to the simulated one of candidate phases with a template matching approach. Since this technique only finds

correlation between the collected patterns and that of the listed candidates, the definition of the candidate bank must be done cautiously. In the present work, it was established based on the Thermo-Calc calculations and XRD analysis (Fig. S1).

Electrical conductivities were measured by the eddy current method with a SIGMATEST 2.069 operating at 60kHz. From these, the thermal conductivities were derived from the Smith-Palmer law [25]. Finally, the macroscopic tensile behaviour was evaluated using dog-bone samples, machined from vertical cylinders to obtain a gauge length of 25 mm and diameter of 4 mm. The room temperature tests were performed according to ISO 6892 standard [26] on a Zwick/Roell Zmart Pro machine equipped with a 100 kN load cell.

The typical tensile response of the stress-relieved and the aged conditions are presented in **Figure 1a, b**, and the derived properties in **Table 2**. A distinct increase in YS of about 140% from the stress-relieved (~130 MPa) to the aged conditions (~310 MPa) is achieved. The strength of the new alloy is superior to that reported for Al-Fe LPBF alloys developed for high conductivity [27,28]. Upon ageing, the electrical and thermal conductivities increased by about 50% (see **Table 2**). The Ashby chart in **Figure 1c** permits to locate the performance of the new Al-Fe-Zr alloy among the cast and wrought Al series with respect to YS and thermal conductivity. High thermal conductivity comes usually at the expense of strength for the conventional alloys, and LPBF materials tend to exhibit intermediate performance, for example AlSi10Mg with YS of 200 MPa and κ of 160 W/m·K when stress-relieved [2]. The Al-Fe-Zr alloy with a YS of 310 MPa and κ of 180 W/m·K after direct ageing of 4 hours at 400°C, will be of interest for heat exchanger applications with complex design requiring both high strength and conductivity. The 6xxx series after a T6 heat-treatment are the only conventional grades with performance approaching the present alloy (see white bubbles in **Figure 1c**). However, as mentioned in the introduction these alloys suffer from poor LPBF-processability and cannot benefit from the associated design freedom.

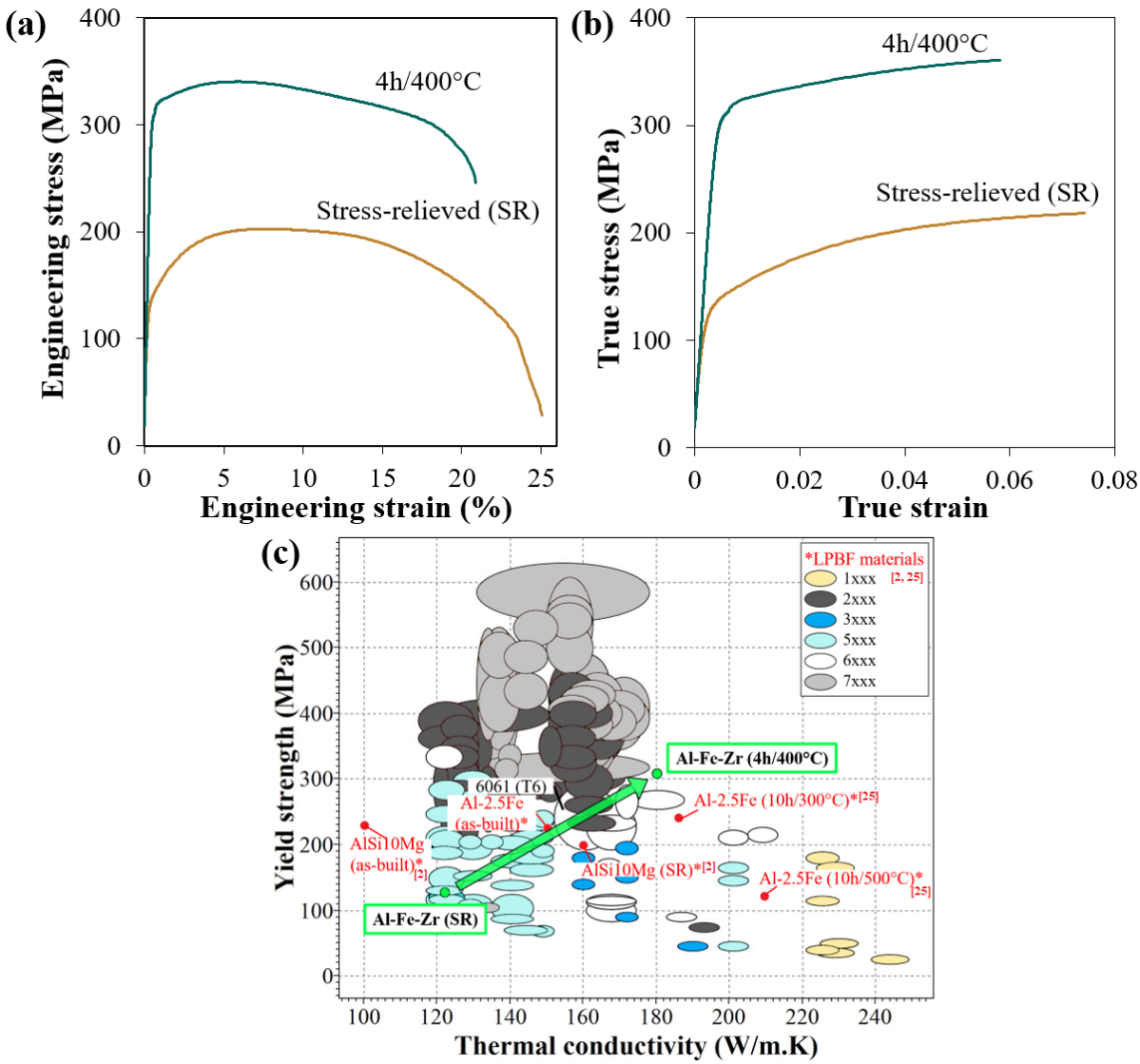


Figure 1: Typical (a) engineering and (b) true tensile stress-strain curves of LPBF Al-Fe-Zr in the stress-relieved (SR) and peak-aged conditions. (c) Ashby chart of yield strength as a function of thermal conductivity plotted with CES Selector GRANTA 2010, showing typical performance of wrought Al alloy series and the novel Al-Fe-Zr introduced in this work.

Condition	YS [MPa]	A [%]	A_u [%]	σ [10^6 S/m]	κ [W/m·K]
SR	128	25	7.2	17.80 ± 0.02	122
4h/400°C	309	13	5.9	27.02 ± 0.02	180

Table 2: Tensile properties (the minimal performances over the conducted 3 tests are reported), electrical σ and thermal conductivity κ of LPBF-processed Al-Fe-Zr in the stress-relieved and peak-aged conditions. Uniform elongation (A_u) is determined just before the test piece necking. Elongation to failure (A) was measured on the engineering stress-strain curves.

An overview of the microstructure along the building direction (BD) for the stress-relieved and the aged material is displayed in **Figure 2**. Large areas including several melt pool boundaries were mapped using EBSD. A complex grain structure is revealed with regions of fine equiaxed grains at the bottom of the melt pools and columnar grains elongated along the BD towards the centre of the melt pools (**Figure 2a** and **d**). These features are common to other Al-alloys developed for LPBF and forming Al_3X-$L1_2$ primary inoculating phases, see e.g.

[8,13]. The grain colouring highlights their weak crystallographic texture. The BSE-SEM images confirm that the alloy is dense, crack-free and well-processed by LPBF.

The presence of fine equiaxed zones (FEZ) displayed in **Figure 2c**, with grains of mean equivalent diameter below 1 µm, is partly attributed to the formation of primary Al_3Zr particles ($L1_2$), leading to heterogeneous nucleation of Al grains at the melt pool boundary where the solid-liquid front velocity is relatively low, as verified using thermal calculations by many authors see e.g. [29–31]. Examples of Al_3Zr with cuboid morphologies are presented in Figure S2.

Towards the centre of the melt pools, the solid-liquid interface velocity increases leading to the suppression of the nucleation of the Al_3Zr particles due to solute trapping, and thus to the columnar growth of Al grains along the local thermal gradient as already shown in [32,33]. The grain structure is stable upon ageing. With a sphericity index threshold at 0.3, the FEZ fraction was estimated to be only in the range of 0.1 to 0.2 in the stress-relieved and aged samples.

In addition, the BSE-SEM images highlight the presence of bright grain boundary particles. Their presence is rather sporadic in the columnar zones (CZ) of the stress-relieved material (~0.3% estimated with ImageJ on **Figure 2b**), while the FEZ grain boundaries appear decorated with thin films and particles (~3% on **Figure 2c**). In the aged condition, both the FEZ and CZ grain boundaries are decorated with coarser bright particles with sizes up to a few hundred nanometres (**Figure 2e and f**).

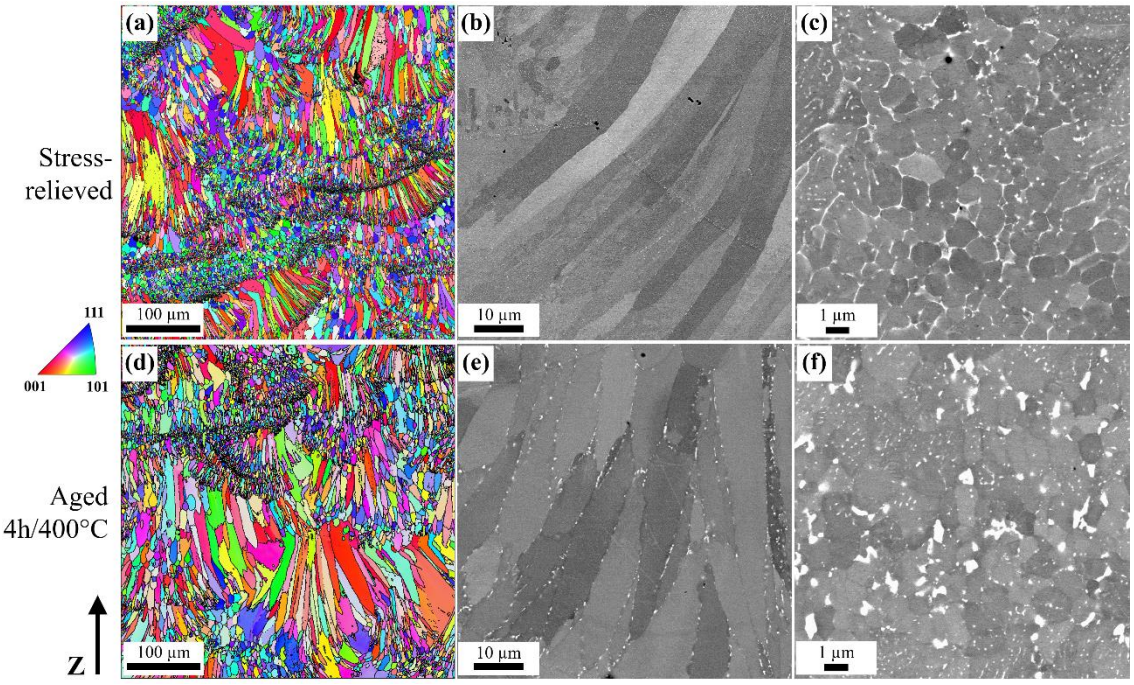


Figure 2: EBSD orientation maps in inverse pole figure (IPF) colouring, (a) in the stress-relieved and (d) the peak-aged (4h at 400°C) conditions. Typical microstructures imaged with the BSE detector within (b, e) the CZ and (c, f) the FEZ.

Using TEM and ACOM, images can be produced by virtually placing apertures of various shapes on the diffraction patterns and integrating the intensity within the aperture for each point on the recorded map. A Virtual Bright Field (VBF) TEM image can be generated with a virtual aperture on the transmitted beam. **Figure 3a** displays a VBF image of a region of interest in the stress-relieved sample containing a grain boundary within a CZ. Experimental

nanodiffraction patterns are displayed overlaid with the best candidate phase. The good agreement between the recorded and simulated templates (**Figure 3f**), together with the consistency with EDS maps (**Figure 3b-e**), identifies the presence of $Al_{13}Fe_4$ (monoclinic), Al matrix and an Al-rich oxide. No Zr-enrichment was found in the second-phase particles. Locally in the stress-relieved sample, metastable Al_6Fe (orthorhombic) could also be identified within the globular Fe-rich intermetallic.

The presence of coarser intergranular Fe-rich precipitates in the aged condition revealed in **Figure 2e-f** suggests the growth and coalescence of the fine globular Fe intermetallics from the stress-relieved sample seen in **Figure 3a**. As shown in [34], the diffusion of Fe in Al matrix is enhanced by the presence of dislocations and grain boundaries. It is also reasonable to assert that the intergranular Fe-rich particles pin the grain boundaries as no substantial change in grain size could be detected in the EBSD maps.

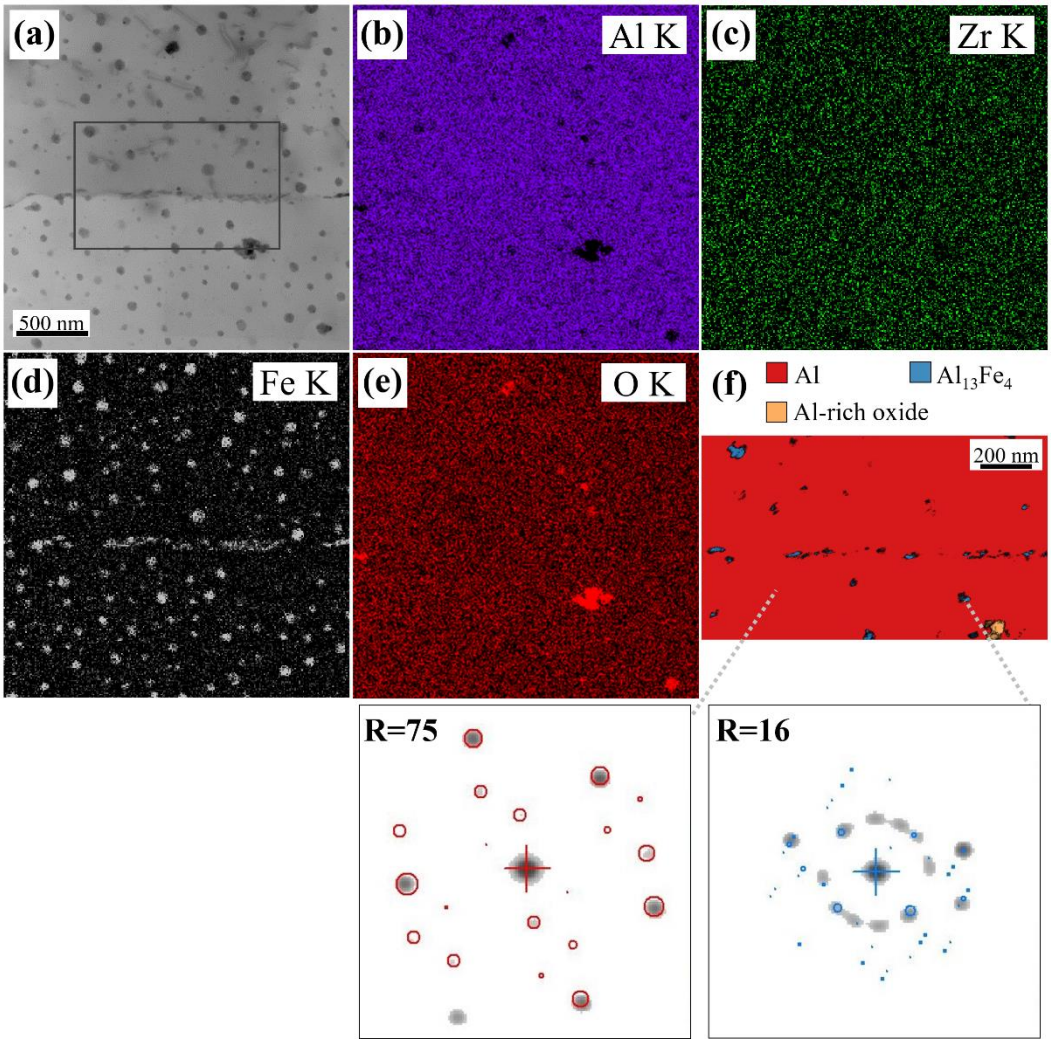


Figure 3: Local solute enrichments and phase distribution of a region of interest containing a grain boundary in the CZ after stress-relief (a) Virtual Bright Field image. EDS maps of the following elements: (b) Aluminium, (c) Zirconium, (d) Iron and (e) Oxygen. (f) Phase map showing the morphology and distribution of phases present within the frame highlighted in (a). The phase reliability in grey scale is overlaid on the map. Selected nanodiffraction patterns are displayed with their corresponding R index.

Figure 4 presents the EDS and ACOM analyses for the aged sample (400°C, 4 hours) within a single grain in a CZ. As for the stress-relieved sample, the globular $Al_{13}Fe_4$ and the

oxide phase are present. Following ageing, high-aspect ratio plate-like $Al_{13}Fe_4$ precipitates are identified, with lengths up to hundreds of nanometres and thicknesses down to a few nanometres. Similarly, as for VBF images, Virtual Dark Field (VDF) images can be generated using virtual apertures integrating the diffracted intensities. Figure S3 generated with such virtual apertures highlights the presence of many crystal orientations within the globular $Al_{13}Fe_4$ particles. These nanocrystals explain the broad XRD peak observed at low angles (Figure S1b). The precipitation of the intragranular plate-like $Al_{13}Fe_4$ is associated with the decomposition of the supersaturated matrix obtained from LPBF. Note that the EDS map shown in **Figure 4c** is not enough resolved to reveal the possible precipitation of Zr-rich nano-sized precipitates. It highlights that despite its low solubility in Al, some Fe is trapped in the solid solution upon LPBF. $Al_{13}Fe_4$ typically leads to large intermetallic particles and embrittlement for cast Al-alloys [35]. Upon LPBF and ageing, the plate-like $Al_{13}Fe_4$ are extremely fine and the material retains good ductility.

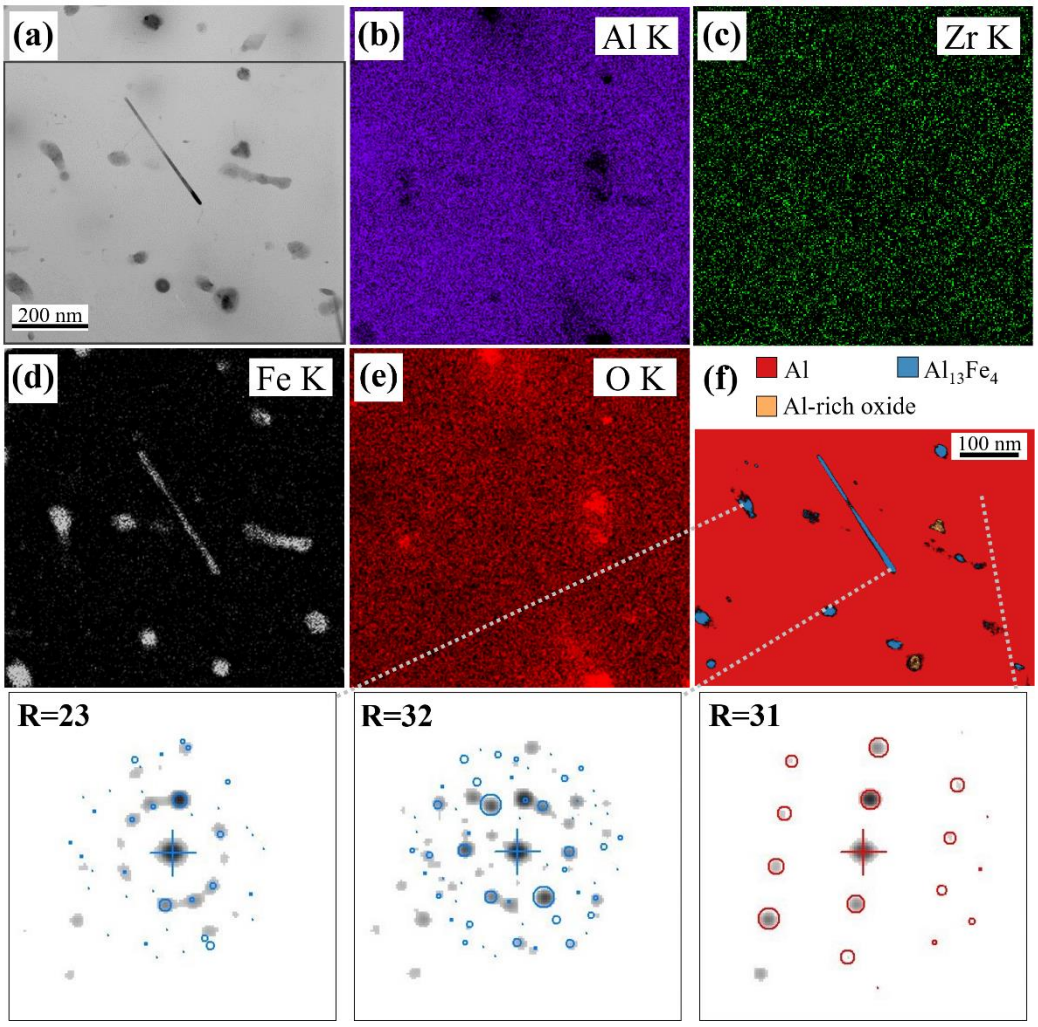


Figure 4: Local solute enrichments and phase distribution of a region of interest in the CZ after ageing at 400°C for 4h. (a) Virtual Bright Field image. EDS maps of the following elements: (b) Aluminium, (c) Zirconium, (d) Iron and (e) Oxygen. (f) Phase map showing the morphology and distribution of phases present within the frame highlighted in (a). The phase reliability in grey scale is overlaid on the map. Selected nanodiffraction patterns are displayed with their corresponding R index.

TEM bright field images and selected area diffraction patterns (SAED) of the aged specimen were collected in a FEZ in <110> zone axis (**Figure 5a, b**) and a CZ in <211> zone

axis (**Figure 5c, d)**, on which are identified the signature of a coherent phase. Fe has a very low solubility in Al and appears to have been consumed by the formation of globular Fe-rich intermetallics upon LPBF and the precipitation of plate-like $Al_{13}Fe_4$ upon ageing. Besides the primary Al_3Zr, no other Zr-rich phases have been identified with ACOM and EDS in the stress-relieved and aged specimens. It is reasonable to propose that the coherent precipitates are spherical nano-sized Al_3Zr as in [13,14]. The high conductivity is attributed to the matrix depletion in solute atoms, namely Fe and Zr, caused by the dual precipitation of $Al_{13}Fe_4$ and Al_3Zr.

Additional ACOM recordings were collected at higher magnification and smaller step size within the matrix. Many of the recorded nanodiffraction patterns exhibit superlattice reflections. The diffracted intensities along a virtual annular aperture where the superlattice reflections are observed (see **Figure 5f**) were used to generate the VDF image in **Figure 5e**. This image reveals the presence of the coherent nanoprecipitates since contrast partly results from the surrounding strain fields. The density of these nano-Al_3Zr appears significantly greater than that of plate-like $Al_{13}Fe_4$ also formed upon ageing. The strengthening associated with the ageing treatment is thus primarily attributed to the nanoprecipitation of coherent Al_3Zr-$L1_2$. To a minor extent, the precipitation of the plate-like $Al_{13}Fe_4$ may additionally contribute to the recorded strengthening.

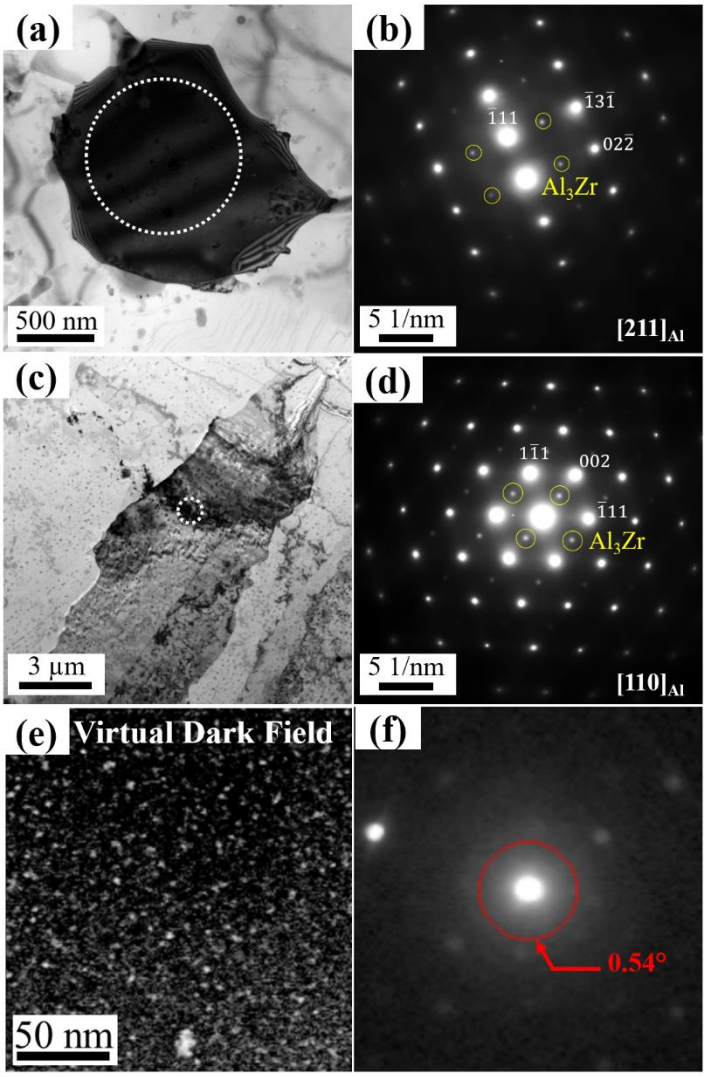


Figure 5: TEM imaging in zone axis of the aged sample: (a, b) bright field image within the FEZ and its associated SAED pattern, (c, d) corresponding image and pattern for the CZ.(e) Virtual Dark Field image within the CZ generated with ACOM and the virtual aperture displayed in (f) on an individual nanodiffraction pattern.

In summary, a novel Al-1Fe-1Zr alloy achieving a superior strength – conductivity trade-off and good LPBF-processability was presented. The primary Al_3Zr ensure no hot cracking occurs, while direct ageing leads to the dual precipitation of coherent nano-Al_3Zr and plate-like $Al_{13}Fe_4$ and YS increase up to 310 MPa. This depletion of the supersaturated matrix obtained from LPBF results in a concomitant conductivity increase.

Declaration of competing interests

The authors declare that they have no known competing financial interests or personal relationships that could have appeared to influence the work reported in this paper.

Acknowledgements

This work has been conducted in the framework of the Aéroprint project supported by La Région Auvergne-Rhône-Alpes. The authors would also like to acknowledge the support from Constellium. Gilles Renou and Patricia Donnadieu are acknowledged for their technical support and fruitful discussions.

References

[1] I.M. Kusoglu, B. Gökce, S. Barcikowski, Addit. Manuf. 36 (2020) 101489.

[2] EOS GmbH, EOS Aluminium AlSi10Mg Material Data Sheet EOS Aluminium AlSi10Mg Good Strength & Dynamic Load Bearing Capacity, 2022.

[3] EOS GmbH, EOS Aluminium AlF357 Material Data Sheet Metal Solutions, 2020.

[4] H. Zhao, D.R. White, T. Debroy, Int. Mater. Rev. 44 (1999) 238–266.

[5] J.H. Martin, B.D. Yahata, J.M. Hundley, J.A. Mayer, T.A. Schaedler, T.M. Pollock, Nature 549 (2017) 365–369.

[6] A. Mehta, L. Zhou, T. Huynh, S. Park, H. Hyer, S. Song, Y. Bai, D.D. Imholte, N.E. Woolstenhulme, D.M. Wachs, Y. Sohn, Addit. Manuf. 41 (2021) 101966.

[7] M. Opprecht, J.P. Garandet, G. Roux, C. Flament, M. Soulier, Acta Mater. 197 (2020) 40–53.

[8] L. Zhou, H. Hyer, S. Park, H. Pan, Y. Bai, K.P. Rice, Y. Sohn, Addit. Manuf. 28 (2019) 485–496.

[9] S.Z. Uddin, L.E. Murr, C.A. Terrazas, P. Morton, D.A. Roberson, R.B. Wicker, Addit. Manuf. 22 (2018) 405–415.

[10] P. Mair, L. Kaserer, J. Braun, N. Weinberger, I. Letofsky-Papst, G. Leichtfried, Mater. Sci. Eng. A 799 (2021) 140209.

[11] T. Gao, S. Zhang, G. Liu, Q. Sun, J. Liu, Q. Sun, J. Sun, Z. Wang, X. Liu, X. Wang, Materialia 16 (2021) 101103.

[12] M. Opprecht, J.P. Garandet, G. Roux, C. Flament, Acta Mater. 215 (2021) 117024.

[13] A.B. Spierings, K. Dawson, P. Dumitraschkewitz, S. Pogatscher, K. Wegener, Addit. Manuf. 20 (2018) 173–181.

[14] A.B. Spierings, K. Dawson, P.J. Uggowitzer, K. Wegener, Mater. Des. 140 (2018) 134–143.

[15] B. Mehta, High Performance Aluminium Alloys for Laser Powder Bed Fusion: Alloy Design and Development, Chalmers University of Technology, 2021.

[16] M. Buttard, B. Chehab, R. Shahani, F. Robaut, G. Renou, C. Tassin, E. Rauch, P. Donnadieu, A. Deschamps, J.J. Blandin, G. Martin, Materialia 18 (2021) 101160.

[17] B. Chebab, S. Unnikrishnan, Met. Addit. Manuf. 8 (2022) 197–201.

[18] J.R. Croteau, S. Griffiths, M.D. Rossell, C. Leinenbach, C. Kenel, V. Jansen, D.N. Seidman, D.C. Dunand, N.Q. Vo, Acta Mater. 153 (2018) 35–44.

[19] B. Forbord, W. Lefebvre, F. Danoix, H. Hallem, K. Marthinsen, Scr. Mater. 51 (2004) 333–337.

[20] Y. Du, Y.A. Chang, B. Huang, W. Gong, Z. Jin, H. Xu, Z. Yuan, Y. Liu, Y. He, F.Y. Xie, Mater. Sci. Eng. A 363 (2003) 140–151.

[21] N.E. Uzan, R. Shneck, O. Yeheskel, N. Frage, Addit. Manuf. 24 (2018) 257–263.

[22] T.M. Mower, M.J. Long, Mater. Sci. Eng. A 651 (2016) 198–213.

[23] E.F. Rauch, M. Véron, Mater. Charact. 98 (2014) 1–9.

[24] A. Després, C. Mayer, M. Veron, E.F. Rauch, M. Bugnet, J.J. Blandin, G. Renou, C. Tassin, P. Donnadieu, G. Martin, Materialia 15 (2021) 101037.

[25] P.G. Klemens, R.K. Williams, Int. Mater. Rev. 31 (2012) 197–215.

[26] DIN EN ISO 6892-1:2016 - Metallic Materials - Tensile Testing - Part 1: Method of Test at Room Temperature, 2017.

[27] X. Qi, N. Takata, A. Suzuki, M. Kobashi, M. Kato, Mater. Sci. Eng. A 805 (2021)

140591.
[28] X. Qi, N. Takata, A. Suzuki, M. Kobashi, M. Kato, J. Mater. Sci. Technol. 97 (2022) 38–53.
[29] N. Raghavan, R. Dehoff, S. Pannala, S. Simunovic, M. Kirka, J. Turner, N. Carlson, S.S. Babu, Acta Mater. 112 (2016) 303–314.
[30] M.S. Pham, B. Dovgyy, P.A. Hooper, C.M. Gourlay, A. Piglione, Nat. Commun. 11 (2020) 1–12.
[31] A. Sonawane, G. Roux, J.J. Blandin, A. Despres, G. Martin, Materialia 15 (2021) 100976.
[32] S. Griffiths, M.D. Rossell, J. Croteau, N.Q. Vo, D.C. Dunand, C. Leinenbach, Mater. Charact. 143 (2018) 34–42.
[33] R.A. Michi, A. Plotkowski, A. Shyam, R.R. Dehoff, S.S. Babu, Int. Mater. Rev. (2021).
[34] A. Duchaussoy, X. Sauvage, K. Edalati, Z. Horita, G. Renou, A. Deschamps, F. De Geuser, Acta Mater. 167 (2019) 89–102.
[35] Z. Song, O. V. Magdysyuk, L. Tang, T. Sparks, B. Cai, J. Alloys Compd. 861 (2021) 158604.